Platinum-Tin Oxide Core-Shell Catalysts for Efficient Electro-Oxidation of Ethanol

7 AUTHORS, INCLUDING:

Wenxin Du
University of New Hampshire
16 PUBLICATIONS   **256** CITATIONS

SEE PROFILE

Guangxing Yang
University of New Hampshire
7 PUBLICATIONS   **122** CITATIONS

SEE PROFILE

Nathaniel Aaron Deskins
Worcester Polytechnic Institute
48 PUBLICATIONS   **1,055** CITATIONS

SEE PROFILE

Dong Su
Brookhaven National Laboratory
187 PUBLICATIONS   **4,003** CITATIONS

SEE PROFILE

Platinum-Tin Oxide Core−Shell Catalysts for Efficient Electro-Oxidation of Ethanol

Wenxin Du,[†] Guangxing Yang,[†] Emily Wong,[†] N. Aaron Deskins,[‡] Anatoly I. Frenkel,[||] Dong Su,[§] and Xiaowei Teng*[,†]

[†]Department of Chemical Engineering, University of New Hampshire, Durham, New Hampshire 03824, United States
[‡]Department of Chemical Engineering, Worcester Polytechnic Institute, Worcester, Massachusetts 01609, United States
[||]Department of Physics, Yeshiva University, New York, New York 10016, United States
[§]Center for Functional Nanomaterials, Brookhaven National Laboratory, Upton, New York 11973, United States

S *Supporting Information*

ABSTRACT: Platinum-tin (Pt/Sn) binary nanoparticles are active electrocatalysts for the ethanol oxidation reaction (EOR), but inactive for splitting the C-C bond of ethanol to CO_2. Here we studied detailed structure properties of Pt/Sn catalysts for the EOR, especially CO_2 generation in situ using a CO_2 microelectrode. We found that composition and crystalline structure of the tin element played important roles in the CO_2 generation: non-alloyed Pt_{46}-$(SnO_2)_{54}$ core−shell particles demonstrated a strong capability for C-C bond breaking of ethanol than pure Pt and intermetallic Pt/Sn, showing 4.1 times higher CO_2 peak partial pressure generated from EOR than commercial Pt/C.

Ethanol is one of the most hopeful fuels renewable energy applications due to its low toxicity, high availability from biomass production, and high energy density due to the 12-electron charge transfer upon complete oxidation.[1] During the ethanol oxidation reaction (EOR), strongly adsorbed intermediates such as CO and CH_x poison the catalyst (e.g., Pt) surface and slow reaction kinetics considerably. Moreover, complete oxidation of ethanol into CO_2 via C-C bond cleavage is mechanistically difficult. Most of the charge generated is from partial oxidation of ethanol to acetaldehyde and/or acetic acid, which only involve a two- or four-electron transfer.[2−7] One common method to improve the performance of Pt for EOR is to use binary catalysts by adding an oxophilic metal, such as Sn.[8,9] Oxophilic metals can facilitate the formation of adsorbed OH species (OH_{ads}) via dissociative adsorption of water, which in turn helps the removal of adsorbed intermediates (CO_{ads}, $CH_{x,ads}$) on adjacent Pt sites (bifunctional effect). Sn also weakens the Pt-CO_{ads} bond by altering d-band properties of Pt orbitals (ligand effect). Although Pt/Sn binary catalysts show improved EOR kinetics, its selectivity for complete oxidation of ethanol to CO_2 is inferior to Pt. Addition of noble metals such as Rh or Ir to Pt has also been studied. The resulting ternary PtRhSn, PtRh-SnO_2, and PtIr-SnO_2 catalysts showed improved reaction kinetics and C-C splitting ability.[5,10−12] However, the scarcity and/or expense of Ir and Rh metals, even compared with Pt, impede their practical applications for fuel cell technology. Therefore, improving C-C splitting of ethanol on the surface of

Pt/Sn catalysts becomes imperative for ethanol fuel cell technology. Many studies investigated Pt/Sn binary catalysts for the EOR; however, factors that may control CO_2 generation on Pt/Sn surface are still not well understood. First, the influence of Sn or SnO_2 on C-C splitting is ambiguous. Adsorption and dissociation of ethanol primarily happen at Pt sites, while Sn or SnO_x provide oxophilic species (OH_{ads}) to remove CO_{ads} and $CH_{x,ads}$. The concentration and distribution of Sn needs to be optimized so that the resulting Pt/Sn catalysts have strong capability for ethanol dissociation (from Pt) and CO/CH_x removal (from Sn) concurrently.[3,13−17] Second, whether Pt-SnO_2 (nonalloys) or PtSn (alloys) would be the best catalyst for EOR kinetics and/or CO_2 generation is still controversial: Antolini, Silva and Jiang reported that Pt-SnO_2 (non-alloys) showed faster EOR kinetics than PtSn (alloys),[3,15,18,19] while De Souza, Zhu, and Godoi reported the opposite results.[14,20−22]

To fundamentally understand the EOR, especially CO_2 generation via C-C splitting, increasing attention has been paid to spectroscopic techniques, e.g., in situ Fourier transform infrared spectroscopy (FTIR) and online differential electrochemical mass spectrometry (DEMS).[2,4,12,13,17,23−27] The former measurement is usually conducted on a thin-layer catalyst surface in stagnant fluid, while the latter uses a flow cell. The experimental results from both techniques were not identical, adding further controversy. For example, FTIR measurements showed that Pt_3Sn catalysts favored the C-C bond splitting in EOR,[2,28,29] in contrast DEMS data showed that CO_2 formation on Pt_3Sn was similar to that on Pt.[3,13,17,30] Ion-selective potentiometric electrodes have been used in aqueous solutions for decades in blood gas analysis and the measurement of CO_2 during fermentation.[24,31] The subject solution and buffer within the electrode are separated by a Teflon membrane which is permeable to dissolved CO_2 gas. The partial pressure of CO_2 gas in the reaction solution can be analyzed via the measurement of the pH of a thin layer of a $NaHCO_3$/NaCl buffer solution within the electrode in equilibrium with CO_2. McGuire reported that a CO_2 microelectrode can enable rapid and continuous measurements of CO_2 concentration in xylem sap of trees.[32] However, implementation of a CO_2 microelectrode to measure the CO_2

generation in situ during electrochemical reactions has not been reported until the current report.

In this work, Pt/Sn nanocrystals were synthesized via a "surfactant-free" Polyol process described by the authors elsewhere.[33] Pt/Sn nanocrystals with an average diameter of <5 nm were harvested as shown from the transmission electron microscopy (TEM) images in Figure 1 (Figure S1 and Table S1).
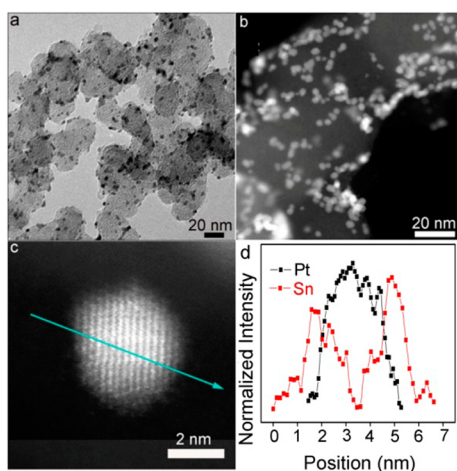

Figure 1. (a) Bright-field TEM, (b) dark-field STEM, and (c) HAADF images of the carbon-supported Pt-SnO$_2$ catalyst. (d) EELS line scan across Pt$_{46}$-(SnO$_2$)$_{54}$ particle as indicated by the arrow in (c).

Two types of Pt/Sn nanoparticles were synthesized with atomic ratios of Pt to Sn as 70/30 and 46/54, respectively (see EDS spectra in Figure S2). The X-ray Diffraction (XRD) pattern shown in Figure S3 indicates mixed phases of pure face centered cubic Pt and tetragonal SnO$_2$ (JCPDS 00-041-1445). To further confirm the structure of the as-made Pt/Sn nanocrystals, high-angle annular dark-field scanning TEM (HAADF-STEM) images (Figure 1c) and electron energy-loss spectroscopy (EELS) line scans (Figure 1d) were generated from an individual Pt-SnO$_2$ nanoparticle. Intensity profiles of Sn and Pt from EELS show that Sn appears to have higher signal intensity at the edges of the particle, in contrast to Pt showing a "volcano" shape of intensity profile. Both the XRD and EELS line scan strongly suggest that as-made Pt/Sn particles were non-alloyed (Pt-SnO$_2$) with a SnO$_2$ shell-rich and Pt core-rich structure.

Figure S4 shows the XANES spectra of Sn K-edge of the non-alloyed Pt-SnO$_2$ catalysts. Pt$_{46}$-(SnO$_2$)$_{54}$ and Pt$_{70}$-(SnO$_2$)$_{30}$ have almost identical spectra that differ strongly from bulk Sn and correspond to the predominantly oxidized state of Sn. This is in good agreement with the results derived from XRD measurements, where the segregated Pt and SnO$_2$ biphases coexisted within Pt-SnO$_2$ non-alloyed samples. EXAFS analysis was also conducted as shown in Figure S5. The best fit values of coordination numbers and bond distances are summarized in Table S2. EXAFS results show that Pt existed mainly in the metallic phase in both non-alloyed Pt-SnO$_2$ samples, as evident in the relatively high Pt-Pt coordination compared to the Pt-O obtained in both samples. Table S2 also shows that Sn is predominantly present in the form of SnO$_2$ in both Pt-SnO$_2$ catalysts, since strong Sn-O coordination number can be observed (N_{Sn-O} = 6.7 ± 1.1 in Pt$_{46}$-(SnO$_2$)$_{54}$ and N_{Sn-O} = 6.0 ± 0.5 in Pt$_{70}$-(SnO$_2$)$_{30}$). Strong Sn-O coordination and nondetectable Sn-Sn and Pt-Sn coordinations corroborate well the XRD and STEM−EELS analyses concluding the as-made Pt-

SnO$_2$ catalysts were comprised of partially oxidized (due to the detectable Pt-O contribution, Table S2) Pt nanoparticles with phase-segregated SnO$_2$ clusters on the surface.

As-made Pt-SnO$_2$ particles were converted into intermetallic compounds after being treated in an Ar/H$_2$ flow at 450 °C. Figures S1 and S3 show their TEM images and XRD spectra. XRD shows that Pt$_{70}$Sn$_{30}$/C has a pure cubic Pt$_3$Sn intermetallic phase (JCPDS 00-035-1360), while the Pt$_{46}$Sn$_{54}$/C catalysts show a mixture of intermetallic cubic Pt$_3$Sn (JCPDS 00-035-1360) and hexagonal Pt$_1$Sn$_1$ alloyed phases (JCPDS 00-025-0614), respectively. No SnO$_2$ reflection was observed from both samples. Figures S6 show the XANES spectra of intermetallic PtSn/C catalysts. Slightly decreased white line intensity of both intermetallic PtSn catalysts compared to Pt foil indicated a lower-lying d-band center relative to the Fermi level, pointing to a more filled d-band. This modified d-band feature may result from electron back-donation from Sn upon alloy formation, which has been previously observed in various Sn-containing noble metal alloys.[33−35] The Sn K-edge XANES features in intermetallic PtSn catalysts are located between those of a Sn foil and non-alloyed Pt-SnO$_2$/C, indicating a mixture of metallic and oxidized phases. EXAFS analyses are shown in Figure S7 and fitting results of the intermetallic alloy are given in Table S2. The Pt atoms showed strong coordination with Sn in Pt$_{46}$Sn$_{54}$ (N_{Pt-Sn} = 2.2 ± 0.3) and Pt$_{70}$Sn$_{30}$ (N_{Pt-Sn} = 1.8 ± 0.3), and the Sn showed strong Sn-Pt coordination and noticeable Sn-O coordination in Pt$_{46}$Sn$_{54}$ ($N_{Sn−Pt}$ = 5.3 ± 0.9, N_{Sn-O} = 3.3 ± 0.8) and Pt$_{70}$Sn$_{30}$ ($N_{Sn−Pt}$ = 9.5 ± 2.1, N_{Sn-O} = 2.9 ± 1.3). Fitting results indicated metallic Sn (in a form of Pt-Sn intermetallic alloy) and trace oxidized Sn (in a form of SnO$_2$) biphase in both intermetallic catalysts.

The electrochemically active surface areas (ECASAs) of non-alloyed and alloyed Pt/Sn catalysts, commercial Pt/C (ETEK), and a mixture of commercial Pt/C with SnO$_2$ nanoparticles are shown in Figure S8, measured using cyclic voltammograms (CVs) in 0.5 M H$_2$SO$_4$. Figure 2 shows EOR electroactivities for Pt/Sn and Pt catalysts in both CV and chronoamperometric (CA) analysis both at 0.35 V. Table S1 and Figure 2b show that the current densities from CV measurements follow the order as Pt$_{70}$Sn$_{30}$ > Pt$_{46}$Sn$_{54}$ > Pt$_{70}$-(SnO$_2$)$_{30}$ > Pt$_{46}$-(SnO$_2$)$_{54}$ > Pt/C (ETEK) ≈ Pt/C + SnO$_2$. Specifically, the Pt$_{70}$Sn$_{30}$/C
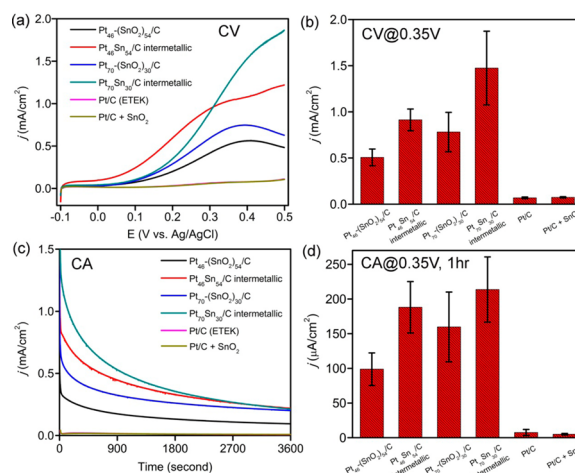

Figure 2. (a) Representative CVs (forward scans) and (b) ECASA-averaged CV current densities of carbon supported Pt/Sn and Pt (ETEK) catalysts at 0.35 V. (c) Representative CAs and (d) ECASA-averaged CA current densities Pt/Sn and Pt/C catalysts at 1 h reaction at 0.35 V.

intermetallic catalyst showed about 21.5 times higher current density at 0.35 V compared to commercial Pt/C. Meanwhile, the ECASA-specific current densities from 1 h CA measurements follow the same order, and the $Pt_{70}Sn_{30}$/C intermetallic showed best long-term stability.

Figure S9 shows the schematic of the electrochemical cell for in situ CO_2 measurement, consisting of a CO_2 microelectrode, Pt foils (working and counter electrode), and Ag/AgCl reference microelectrode. Pure argon and nitrogen gases mixed with 0.5, 1, and 5% CO_2 were used to calibrate the CO_2 microelectrodes in an electrolyte solution at 25 °C (Figure 3a). The generation of
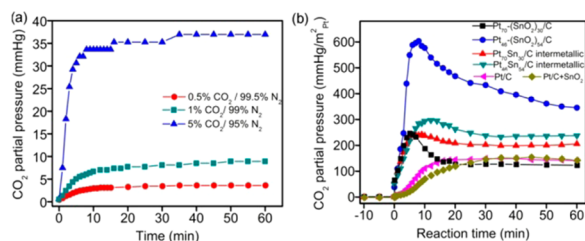

Figure 3. (a) CO_2 microelectrode responses in various CO_2 gas environments. (b) ECASA-specific P_{CO_2} of Pt/Sn and Pt catalysts.

CO_2 on Pt/Sn and commercial Pt/C catalysts was evaluated in situ using an electrochemical cell applied with a constant potential of 0.35 V. Figure 3b shows the plot of the partial pressure of CO_2 (P_{CO_2}), normalized by ECASA values, as a function of reaction time. The results are also summarized in Table S1. Pt_{46}-$(SnO_2)_{54}$/C demonstrated the best CO_2 generation ability compared to the rest of Pt/Sn and Pt catalysts. In particular, maximum CO_2 generation found in Pt_{46}-$(SnO_2)_{54}$/C was 2.0 and 4.1 times higher than those found in its intermetallic counterpart and Pt/C (ETEK). At steady state (after 1 h reaction), Pt_{46}-$(SnO_2)_{54}$/C still showed at least 1.5 and 2.5 times higher P_{CO_2} compared to $Pt_{46}Sn_{54}$/C and Pt/C, respectively. In contrast to Pt_{46}-$(SnO_2)_{54}$/C and $Pt_{46}Sn_{54}$ catalysts, from which the core−shell particles outperform the intermetallic particles in CO_2 generation, the $Pt_{70}Sn_{30}$ generated more CO_2 than Pt_{70}-$(SnO_2)_{30}$/C during the EOR. The results strongly indicated that CO_2 generation abilities of various Pt/Sn catalysts were more dependent on the composition of Sn than crystalline structure (alloys or non-alloy).

Figure S10 shows the long-term stability of Pt_{46}-$(SnO_2)_{54}$ and Pt (ETEK) at lower potentials (0.1 and 0.2 V). Pt_{46}-$(SnO_2)_{54}$ shows a steady current after 1 h reaction at 0.2 V, while Pt remains negative current during the reaction due to the dominant cathodic current from hydrogen absorption. The data indicate that Pt_{46}-$(SnO_2)_{54}$ not only has a good stability at lower potentials but also has a lower onset potential for the EOR compared to Pt. Figure S11 shows CO_2 generations of Pt_{46}-$(SnO_2)_{54}$ and Pt (ETEK) after 1 h CA measurements conducted at 0.1 and 0.2 V. Combined with Figure 3b, it clearly shows: (i) both catalysts yield more CO_2 at higher potentials; and (ii) Pt_{46}-$(SnO_2)_{54}$ remains a plausible ability to generate CO_2 at lower potentials, showing 9.6, 5.3, and 2.5 times higher P_{CO_2} compared to Pt at 0.1, 0.2, and 0.35 V, respectively.

Acetic acid (AA) and acetaldehyde (AAL) have been identified as major products during EOR. As shown in Figure S12, the measured P_{CO_2} was attributed from dissolved CO_2 only and the interference from AA and AAL generated during the EOR to the P_{CO_2} was negligible (see Supporting Information (SI) for details).

We also modeled the decomposition of CHCO over Pt (111), PtSn($11\bar{2}0$), and Pt/SnO_2 interfaces using density functional theory (DFT). Details on the calculations are found in the SI. C-C bond breaking can occur through a variety of intermediates that form after C−H/C−O bond breaking. Previous theoretical work indicated over Pt (111) that C-C bond breaking of ethanol has one of the lowest activation barriers through a CHCO intermediate.[36] Other pathways may be possible for C-C breaking, but this species was chosen as a representative intermediate to assess ethanol oxidation ability. For each surface several adsorption sites were considered. For instance, adsorption at the Pt/SnO_2 surface was modeled over SnO_2, over the (111) facets of the Pt, and in the Pt/SnO_2 interfacial region. Only the most stable adsorption sites are reported herein and were considered for evaluating the reaction energy for C-C scission. Figure S13 shows the DFT results for CHCO decomposition to CO and CH over the various surfaces of interest. We calculated reaction energies (energies of product states minus reactant states) for CHCO decomposition to be −1.04 eV over Pt (111), −0.19 eV over Pt/SnO_2, and 0.36 eV over PtSn. These results indicate that breaking C-C bond is the easiest over Pt, followed by Pt/SnO_2, and then PtSn. These simple calculations indicate that Pt/SnO_2 is better able to break C-C bond compared to PtSn, in agreement with an experiment that shows greater CO_2 production for Pt/SnO_2 catalysts. Thus, we expect PtSn to behave much different than Pt/SnO_2 as an ethanol oxidation catalyst. While Pt performs best for C-C bond breaking, a full reaction path analysis is needed to explain its overall activity, which is experimentally inferior.

We here discuss two possibilities to explain the physical origin of promotional effect of Pt_{46}-$(SnO_2)_{54}$/C core−shell structures on C-C splitting observed in this study. First, concentration of SnO_2 is imperative for C-C splitting. In the primary path of EOR (black arrows in Figure S14), weakly bound AAL forms on Pt surfaces at lower potentials. It can readily desorb from the surface of catalysts or it can be oxidized further to form AA as primary products in the EOR, which are very inert in electrocatalysis. Meanwhile, AAL can possibly be further reacted to form C_1 intermediates (CO, CH_x) via C-C bond cleavage and eventually oxidized to CO_2 ($CH_3CH_2OH \rightarrow CH_3CHO \rightarrow CH_x + CO \rightarrow CO_2$).[37] Therefore, OH_{ads}, formed via dissociative adsorption of water at Sn sites, is needed in order to oxidize CO_{ads} and $CH_{x,ads}$ at adjacent sites to promote CO_2 generation. On the other hand, complete oxidation of ethanol to form CO_2 is more facile on Pt sites. Our data suggest strongly that Pt_{46}-$(SnO_2)_{54}$ is the best catalyst for CO_2 generation (See Figure S15a), so that CO_{ads} and $CH_{x,ads}$ can be effectively removed, and at the same time, the ethanol dissociation is not compromised.

Second, size or coverage of SnO_2 clusters may play an important role in CO_2 generation. It was found that 2 nm SnO_2 nanoparticles on Pt electrode surfaces showed much higher enhancement of methanol oxidation reaction current densities compared to Pt decorated with larger SnO_2 nanoparticles.[38] DFT calculations suggest that the binding energy of OH_{ads} on the surface of SnO_2 nanoparticles depended on the sizes of SnO_2. Small-sized SnO_2 nanoparticles on Pt surface would have a weaker OH-Sn interaction, and favor the release of OH_{ads} from the SnO_2 surface for effectively oxidizing CO_{ads}. We found that pure Pt/C and the mixture of Pt/C and SnO_2 nanoparticles (commercial product) had very similar EOR kinetics and C-C splitting ability, both inferior to $Pt-SnO_2$ and PtSn as shown in Figures 2 and 3 (labeled as Pt/C + SnO_2), suggesting that close proximity of Pt and SnO_2 is critical to enhance the CO_2

10864

dx.doi.org/10.1021/ja505456w | *J. Am. Chem. Soc.* 2014, 136, 10862−10865

generation. To further elucidate the effect of SnO_2 on CO_2 generation, we calculated the SnO_2 coverage and SnO_2 coverage/Pt coverage on the surfaces of various Pt-SnO_2 catalysts using ECASAs (see detailed description in SI). Figure S15b,c shows the CO_2 generation on various Pt-SnO_2 catalysts as functions of SnO_2 coverage and SnO_2 coverage/Pt coverage on surface. We found that SnO_2 coverage/Pt coverage on surface of Pt_{46}-$(SnO_2)_{54}$ is around 2.4, accounting for 71% SnO_2 on surface.

The results from our work, including time-resolved CO_2 generation using a CO_2 microelectrode, the influences of structures (core−shell and alloy) and compositions on the CO_2 generation, and DFT modeling of C-C splitting on various Pt/Sn structures, have demonstrated that, for the first time, Pt_{46}-$(SnO_2)_{54}$ core−shell nanoparticles can effectively generate CO_2 via splitting C-C bond of ethanol. Our data show that Pt_{46}-$(SnO_2)_{54}$ electrocatalysts have 9.6, 5.3, and 2.5 times higher amount of CO_2 generation compared to Pt (ETEK) after 1 h reaction at 0.1, 0.2, and 0.35 V, respectively. We notice that sample environments for in situ CO_2 determination are very different in CO_2 microelectrode, FTIR, and DEMS techniques. Comparison of CO_2 generation between these three techniques will be challenging but will be the focus of our future work. Nevertheless, our results unambiguous demonstrate the potential of CO_2 microelectrode as a low-cost, easy-to-use, high-performance in situ tool for the CO_2 detection in electrochemical processes, compared to other optical- and mass spec-electrochemical techniques.

ASSOCIATED CONTENT

Supporting Information
Detailed description of the materials syntheses and characterizations, EDS, XRD, XANES, and EXAFS spectra and design of in situ cell for CO_2 measurements. This material is available free of charge via the Internet at http://pubs.acs.org.

AUTHOR INFORMATION

Corresponding Author
xw.teng@unh.edu

Notes
The authors declare no competing financial interest.

ACKNOWLEDGMENTS

REFERENCES

(1) Lave, L. B.; Griffin, W. M.; MacLean, H. *Issues Sci. Technol.* **2001**, *18*, 73.
(2) Vigier, F.; Coutanceau, C.; Hahn, F.; Belgsir, E. M.; Lamy, C. *J. Electroanal. Chem.* **2004**, *563*, 81.
(3) Jiang, L.; Colmenares, L.; Jusys, Z.; Sun, G. Q.; Behm, R. J. *Electrochim. Acta* **2007**, *53*, 377.
(4) De Souza, R. F. B.; Parreira, L. S.; Silva, J. C. M.; Simoes, F. C.; Calegaro, M. L.; Giz, M. J.; Camara, G. A.; Neto, A. O.; Santos, M. C. *Int. J. Hydrogen Energy* **2011**, *36*, 11519.
(5) Kowal, A.; Li, M.; Shao, M.; Sasaki, K.; Vukmirovic, M. B.; Zhang, J.; Marinkovic, N. S.; Liu, P.; Frenkel, A. I.; Adzic, R. R. *Nat. Mater.* **2009**, *8*, 325.
(6) Antolini, E.; Gonzalez, E. R. *J. Power Sources* **2010**, *195*, 3431.
(7) Liu, H. S.; Song, C. J.; Zhang, L.; Zhang, J. J.; Wang, H. J.; Wilkinson, D. P. *J. Power Sources* **2006**, *155*, 95.
(8) Lamy, C.; Belgsir, E. M.; Leger, J. M. *J. Appl. Electrochem.* **2001**, *31*, 799.
(9) Zhou, W. J.; Zhou, Z. H.; Song, S. Q.; Li, W. Z.; Sun, G. Q.; Tsiakaras, P.; Xin, Q. *Appl. Catal., B* **2003**, *46*, 273.
(10) Li, M.; Kowal, A.; Sasaki, K.; Marinkovic, N.; Su, D.; Korach, E.; Liu, P.; Adzic, R. R. *Electrochim. Acta* **2010**, *55*, 4331.
(11) Du, W. X.; Wang, Q.; LaScala, C. A.; Zhang, L. H.; Su, D.; Frenkel, A. I.; Mathur, V. K.; Teng, X. W. *J. Mater. Chem.* **2011**, *21*, 8887.
(12) Li, M.; Cullen, D. A.; Sasaki, K.; Marinkovic, N. S.; More, K.; Adzic, R. R. *J. Am. Chem. Soc.* **2013**, *135*, 132.
(13) Wang, H.; Jusys, Z.; Behm, R. J. *J. Power Sources* **2006**, *154*, 351.
(14) De Souza, R. F. B.; Parreira, L. S.; Rascio, D. C.; Silva, J. C. M.; Teixeira-Neto, E.; Calegaro, M. L.; Spinace, E. V.; Neto, A. O.; Santos, M. C. *J. Power Sources.* **2010**, *195*, 1589.
(15) Jiang, L. H.; Zhou, Z. H.; Li, W. Z.; Zhou, W. J.; Song, S. Q.; Li, H. Q.; Sun, G. Q.; Xin, Q. *Energy Fuels* **2004**, *18*, 866.
(16) Colmati, F.; Antolini, E.; Gonzalez, E. R. *J. Power Sources.* **2006**, *157*, 98.
(17) Wang, Q.; Sun, G. Q.; Jiang, L. H.; Xin, Q.; Sun, S. G.; Jiang, Y. X.; Chen, S. P.; Jusys, Z.; Behm, R. J. *Phys. Chem. Chem. Phys.* **2007**, *9*, 2686.
(18) Antolini, E.; Colmati, F.; Gonzalez, E. R. *J. Power Sources* **2009**, *193*, 555.
(19) Silva, J. C. M.; De Souza, R. F. B.; Parreira, L. S.; Neto, E. T.; Calegaro, M. L.; Santos, M. C. *Appl. Catal., B* **2010**, *99*, 265.
(20) Zhu, M. Y.; Sun, G. Q.; Yan, S. Y.; Li, H. Q.; Xin, Q. *Energy Fuels* **2009**, *23*, 403.
(21) Godoi, D. R. M.; Perez, J.; Villullas, H. M. *J. Power Sources.* **2010**, *195*, 3394.
(22) Silva, J. C. M.; Parreira, L. S.; De Souza, R. F. B.; Calegaro, M. L.; Spinace, E. V.; Neto, A. O.; Santos, M. C. *Appl. Catal., B* **2011**, *110*, 141.
(23) Iwasita, T.; Rasch, B.; Cattaneo, E.; Vielstich, W. *Electrochim. Acta* **1989**, *34*, 1073.
(24) Perez, J. M.; Beden, B.; Hahn, F.; Aldaz, A.; Lamy, C. *J. Electroanal. Chem.* **1989**, *262*, 251.
(25) Iwasita, T.; Pastor, E. *Electrochim. Acta* **1994**, *39*, 531.
(26) Wang, H.; Jusys, Z.; Behm, R. J. *Fuel Cells.* **2004**, *4*, 113.
(27) Shao, M. H.; Adzic, R. R. *Electrochim. Acta* **2005**, *50*, 2415.
(28) Leger, J. M.; Rousseau, S.; Coutanceau, C.; Hahn, F.; Lamy, C. *Electrochim. Acta* **2005**, *50*, 5118.
(29) Leger, J. M. *Electrochim. Acta* **2005**, *50*, 3123.
(30) Colmenares, L.; Wang, H.; Jusys, Z.; Jiang, L.; Yan, S.; Sun, G. Q.; Behm, R. J. *Electrochim. Acta* **2006**, *52*, 221.
(31) Severinghaus, J. W.; Bradley, A. F. *J. Appl. Physiol.* **1958**, *13*, 515.
(32) McGuire, M. A.; Teskey, R. O. *Tree Physiol.* **2002**, *22*, 807.
(33) Du, W. X.; Wang, Q.; Saxner, D.; Deskins, N. A.; Su, D.; Krzanowski, J. E.; Frenkel, A. I.; Teng, X. W. *J. Am. Chem. Soc.* **2011**, *133*, 15172.
(34) Jiang, L. H.; Sun, G. Q.; Sun, S. G.; Liu, J. G.; Tang, S. H.; Li, H. Q.; Zhou, B.; Xin, Q. *Electrochim. Acta* **2005**, *50*, 5384.
(35) Neto, A. O.; Dias, R. R.; Tusi, M. M.; Linardi, M.; Spinace, E. V. *J. Power Sources* **2007**, *166*, 87.
(36) Alcala, R.; Mavrikakis, M.; Dumesic, J. A. *J. Catal.* **2003**, *218*, 178.
(37) Neurock, M. *Handbook of Fuel Cells: Fundamentals, Technology, and Applications*; John Wiley & Sons: Hoboken, NJ, 2003; Vol. 4, p 152.
(38) Zhou, W. P.; An, W.; Su, D.; Palomino, R.; Liu, P.; White, M. G.; Adzic, R. R. *J. Phys. Chem. Lett.* **2012**, *3*, 3286.